# Elucidating the local atomic and electronic structure of amorphous oxidized superconducting niobium films

Thomas F. Harrelson,[1,2] Evan Sheridan,[1,2,3] Ellis Kennedy,[4] John Vinson,[5] Alpha T. N'Diaye,[6] M. Virginia P. Altoé,[2] Adam Schwartzberg,[2] Irfan Siddiqi,[1,7] D. Frank Ogletree,[2] Mary C. Scott,[4,8] and Sinéad M. Griffin[1,2,a)]

[1)] *Materials Science Division, Lawrence Berkeley National Laboratory, Berkeley, CA 94720, USA*

[2)] *Molecular Foundry, Lawrence Berkeley National Laboratory, Berkeley, CA 94720, USA*

[3)] *Theory and Simulation of Condensed Matter, Department of Physics, King's College London, The Strand, London WC2R 2LS, UK.*

[4)] *Department of Materials Science and Engineering, University of California, Berkeley, CA 94720, USA*

[5)] *Material Measurement Laboratory, National Institute of Standards and Technology, Gaithersburg, MD 20899, USA*

[6)] *Advanced Light Source, Lawrence Berkeley National Laboratory, Berkeley, CA 94720, USA*

[7)] *Department of Physics, University of California, Berkeley, CA 94720, USA*

[8)] *NCEM, Molecular Foundry, Lawrence Berkeley National Laboratory, Berkeley, CA 94720, USA*

Qubits made from superconducting materials are a mature platform for quantum information science application such as quantum computing. However, materials-based losses are now a limiting factor in reaching the coherence times needed for applications. In particular, knowledge of the atomistic structure and properties of the circuit materials is needed to identify, understand, and mitigate materials-based decoherence channels. In this work we characterize the atomic structure of the native oxide film formed on Nb resonators by comparing fluctuation electron microscopy experiments to density functional theory calculations, finding that an amorphous layer consistent with an $Nb_2O_5$ stoichiometry. Comparing X-ray absorption measurements at the Oxygen K edge with first-principles calculations, we find evidence of *d*-type magnetic impurities in our sample, known to cause impedance in proximal superconductors. This work identifies the structural and chemical composition of the oxide layer grown on Nb superconductors, and shows that soft X-ray absorption can fingerprint magnetic impurities in these superconducting systems.

Superconducting qubits are one of the leading solid-state platforms for QIS (quantum information science) applications, with reported coherence times reaching ∼100 microseconds.[1,2] Despite this, materials-based decoherence channels contribute significantly to microwave losses, and are now a central hurdle in device coherence and scaling.[3] In particular, the inevitable inhomogeneities that are present from growth and fabrication, such as interfaces, defects, and structural disorder, each contribute to the decoherence in qubits amde from superconducting materials.[4,5]

Precise knowledge of the atomistic structural and chemical makeup of superconducting qubit materials is particularly necessary for understanding materials-dependent decoherence processes. Intrinsic noise sources in superconducting qubits are typically classified into two categories – two-level system (TLS) noise, and non-TLS noise.[6] TLSs are fluctuating two-level states comprising local energy minima in the atomic structural potential which were originally proposed to describe the microstructure of amorphous materials.[7] TLSs can couple to electric and magnetic fields, reducing a qubit's coherence time. Since the amorphous materials present on superconducting qubit surfaces consist of a variety of bonding environments, TLSs can host a range of barrier heights and tunnelling rates, and correspondingly a distribution of fluctuation frequencies even within a given material.[8] Because of this, characterization of the local atomic arrangements is needed to build any predictive description of TLS-related decoherence.

Non-TLS noise intrinsic in QIS materials includes the presence of nonequilibrium quasiparticles (QP)[9,10] and of magnetic impurities.[11–13] While careful shielding can mitigate some of these effects, the decay and control of QPs is materials dependent, and can be crucially influenced by nanofabrication and materials' control.[9,14,15] Another key non-TLS loss mechanism is Cooper pair breaking induced by the presence of magnetic impurities,[11] which can occur due to materials' defects, interfaces, and surfaces, and cause impedance losses in the superconductor.[11–13] Therefore, to understand the structure-coherence relationships associated with the materials' properties in superconducting qubits, knowledge of the local structural and chemical environment is needed, regardless of the origin (TLS, non-TLS) of the noise.

Superconducting qubits are typically comprised of $Al/AlO_x/Al$ Josephson junctions with superconducting

[a)] Author to whom correspondence should be addressed: sgriffin@lbl.gov

circuit elements commonly made from Al, Nb, Ta, and alloys containing these.[4,16] Of these, Nb has many advantages over other superconducting materials including low kinetic inductance resulting in reduced variability, and a higher superconducting gap making it less susceptible to QP poisoning.[17] Importantly, Nb forms a relatively clean surface, and is a mature material for the advanced processing and lithographic patterning that is required for contemporary qubit fabrication and for future scaling of highly coherent superconducting architectures. However, Nb readily forms surface oxides such as NbO, $NbO_2$ and $Nb_2O_5$, which introduce both TLS and non-TLS losses in the qubit.[18,19] Previous work has looked at the use of ultrahigh vacuum packing to reduce surface contamination,[20] in addition to an understanding of the influence of both oxide surface removal[19] and regrowth[21] on the performance of superconducting resonators.

Despite extensive research on the variety of loss channels and their mitigation through surface treatments and fabrication,[22,23] the precise microscopic origins of TLS and non-TLS losses in superconducting systems is not known. This is primarily due to the difficulty in accessing information about the local structural and chemical environments which critically control the presence of these losses. Since the native oxides formed on Nb are often amorphous, conventional diffraction and computational techniques cannot be used for structural information. Theoretical treatments often either rely on having crystalline materials with periodic boundary conditions,[24] or propose phenomenological models without incorporating nanoscale structural information. Instead, in this work, we combine Fluctuation Electron Microscopy (FEM), X-Ray Absorption Spectroscopy (XAS), and first-principles calculations to investigate the structural and chemical composition of amorphous oxides on superconducting Nb films. We classify the short- and mid-range structural properties of our oxides by comparing our *ab initio* calculations with experiments, identifying the structural and chemical makeup of surface Nb oxides on superconducting resonators.

To characterize the mid-range atomic structure of the amorphous films we used FEM, a 4-D scanning transmission electron microscopy technique that is sensitive to medium-range atomic ordering in disordered materials.[25] FEM experiments were performed using an FEI TitanX operated at an acceleration voltage of 200 kV. Additionally, XAS measurements of the O K-edge were performed at the bending magnet beamline 6.3.1 at the Advanced Light Source at Lawrence Berkeley National Laboratory. We consider three different Nb treatments: (1) unpatterned, oxidized Nb films without any treatments, (2) Nb film from a chip patterned with qubits, and (3) Nb film from a chip with resonators only (no Josephson junctions), which allows us to potentially observe changes in the Nb oxides with these different fabrication steps (Table I). XAS was performed on all three samples. FEM was performed on Sample 2 because it had the thickest oxide layer, which was required for improved signal

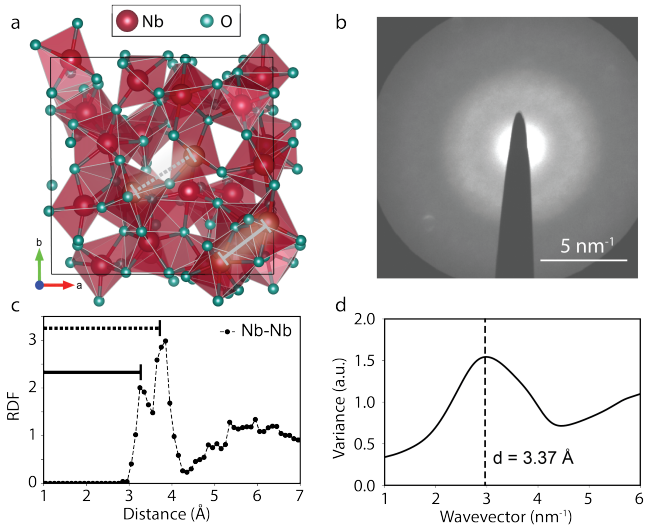


FIG. 1. (a) Representative *ab initio* molecular dynamics generated amorphous structure of $Nb_2O_5$. (b) Averaged speckle pattern of $Nb_2O_5$ using FEM over many diffraction patterns. (c) Radial Distribution Function for $Nb_2O_5$ obtained from averaging over nine amorphous stoichiometric configurations generated using *ab initio* molecular dynamics, (d) Annular mean of normalized variances of the FEM data measuring the average interatomic spacing between Nb centers in the $Nb_2O_5$.

in FEM analysis. Further details of the FEM and XAS measurements are given in the SI.

Electronic and magnetic properties were calculated using density functional theory (DFT) as implemented in the Vienna Ab initio Simulation Package (VASP).[26] We used $Nb_2O_5$ amorphous structures that were generated previously with *ab initio* molecular dynamics as detailed in Ref.,[13] which are available on Zenodo.[27] X-ray absorption calculations were carried out using the Bethe-Salpeter equation (BSE) formalism as implemented within the OCEAN code.[28] The BSE calculations use a basis of electron orbitals from DFT calculated with QUANTUM ESPRESSO,[29] with pseudopotentials from the PseudoDojo collection.[30,31] More details on the DFT and XAS calculations are given in the SI.

We first describe our FEM diffraction results of a representative oxidized Nb sample with the largest oxide thickness (Sample 2), and compare the short-range structural description to *ab initio* generated structures. In contrast to other diffraction techniques, which generally identify long-range ordering, FEM is uniquely sensitive to the medium-range ordering on the size scale of the electron beam probe.[32,33] FEM data is acquired by rastering a small electron probe over a sample and capturing a diffraction pattern at each probe location. The diffraction patterns are digitally preprocessed to remove imaging distortions, and the variance of the measured intensity as a function of scattering vector is calculated.[34] As Bragg scattering in the diffraction patterns creates

large variance in intensity, the calculated variance is a metric for ordering in the amorphous material on the length scale of the electron probe.[35] Full details of the FEM method and data analysis are given in the SI. In Figure 1(b), we show the average speckle pattern of many nanodiffraction patterns taken over the Nb oxide region of the film cross-section (see SI). The brighter spots in the speckled halo primarily represent Nb-Nb distances because electron scattering from Nb atoms dominates over scattering from O atoms. The broad diffuse halo present in the average nanodifraction pattern suggests that the Nb oxide film is amorphous. In Figure 1(d) we show an average spatial variance computed from six regions of the sample, where each region differs in its thickness, as shown in Figure S1 of the Supplementary material. The broad peak centered at the wavevector ≈3 $nm^{-1}$ is a measure of the average interatomic spacing between Nb centres, corresponding to an average Nb-Nb distance of 3.37 Å.

We next analyze *ab initio*-generated amorphous structures to investigate the short- and medium-range structural order across a sample of stoichiometric $Nb_2O_5$ amorphous configurations. Figure 1(a) illustrates a representative stoichiometric amorphous configuration of $Nb_2O_5$ containing 105 atoms in the unit cell. The solid line indicates the Nb-Nb distance for edge sharing Nb sites in $Nb_2O_5$, while the dashed line highlights the longer Nb-Nb distances for corner sharing Nb sites. These features are also present in Figure 1(c), where we show the averaged radial distribution function (RDF) obtained from nine stoichiometric amorphous configurations of $Nb_2O_5$ whose volume and internal coordinates were optimized using DFT. We see from the first peak that the shorter edge sharing Nb sites are typically 3.15 Å apart, and the longer corner sharing Nb sites are 3.8 Å apart as indicated by the second peak. The immediate dip of the RDF at 4 Å suggests that the edge- and corner-sharing environments shown in Figure 1(a) are the primary structural motifs present in our amorphous $Nb_2O_5$. Given the reasonable comparison between *ab initio*-generated amorphous structures and FEM analysis of our Nb oxide thin films, we can conclude that indeed our films are amorphous, lacking any long-range order, and that our generated structures can be used for further analysis. Additionally, we find the average Nb-Nb distance in the FEM measurement to be 3.37 Å, which is between the average corner- and edge-shared Nb-Nb distances in the *ab initio* structures, suggesting our amorphous films comprise a mix of corner- and edge-sharing polyhedra.

We next use X-ray absorption spectroscopy (XAS) to obtain information about the local morphology, electronic structure, and potential magnetism. We focus on O K-edge spectra for three different $NbO_x$ samples, which are described in Table I. While XAS of the O K edge probes unoccupied *p*-type states surrounding the oxygen atoms, these states are hybridized with the neighboring Nb, and so provide information on both the Nb and O species. In Figure 2 we plot the measured XAS

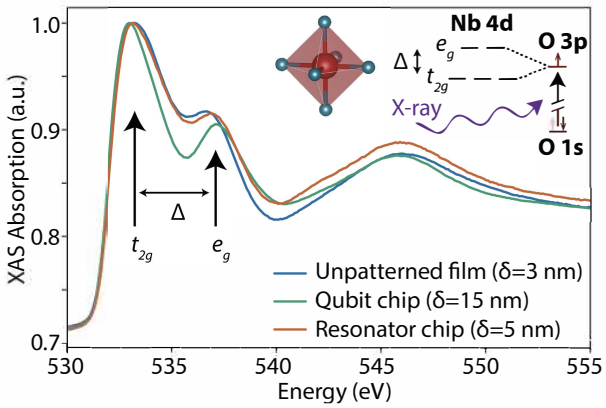


FIG. 2. Measured XAS spectra of O K-edge for the three different samples described in Table I. Inset: Sketch of the electronic structure of octahedrally coordinated Nb forming $t_{2g}$ and $e_g$ split orbital sets. These hybridize with the unoccupied O orbitals that are excited upon X-ray absorption, creating the observed splitting between the peaks in the data. Spectra were normalized by matching the baselines, and dividing by the maximum value in the 525 eV to 550 eV window.

| Sample | $NbO_x$ Thickness | Description |
|---|---|---|
| 1 | 3 nm | Unpatterned, oxidized Nb film. |
| 2 | 15 nm | Nb film fabricated with qubits including $AlO_x$ Josephson junctions. |
| 3 | 5 nm | Nb film fabricated with resonators only (no Josephson junctions). |

TABLE I. Summary of sample details used in experiments. XAS measurements were performed on all three samples, whereas FEM measurements were performed on Sample 2.

for the three samples, and find the XAS is similar for all three. As is typical in transition metal oxides, we identify the two peaks at 533 eV and 537 eV as hybridized with the empty Nb *4d* orbitals, split by the crystal field splitting Δ into lower-energy $t_{2g}$ and higher-energy $e_g$ states. The broad feature near 544 eV reflects hybridization with Nb *5sp*-like states. Changes in the relative intensities of the $t_{2g}$ and $e_g$, and splitting between them Δ, and (less reliably) position of the edge onset, reflect changes in the Nb *d*-manifold occupation, strength of the Nb-O bonding, and oxidation state of the metal ion, respectively.[36]

Comparing the XAS spectra of the three measured samples shows that the unpatterned film (Sample 1) and the resonator chip (Sample 3) are the most similar. We observe a slight increase in energy of the peak near 537 eV, and the slight increase in intensity of the broad feature near 544 eV for the resonator sample (Sample 3) compared to the unpatterned sample (Sample 1). The qubit sample (Sample 2) has the largest $NbO_x$ thickness (∼ 15 nm), and largest increase in energy of the 537 eV peak. The observed increase in the energy of the 537 eV peak in the patterned samples suggests a greater crystal-field splitting hence more crystalline character compared

to the unpatterned films.

We use a combination of DFT and BSE calculations to further analyze the XAS spectra. We calculate spectra for fifteen different $Nb_2O_5$ amorphous configurations (both stoichiometric and non-stoichiometric), and five different crystalline phases of Nb-oxides. In Figure 3(a), we plot the calculated crystalline spectra for NbO ($Pm3m$), $NbO_2$ ($P4_2/mnm$), and the average of 3 different $Nb_2O_5$ phases (N-phase ($C_2/m$), M-phase ($I4/mmm$), and B-phase ($C_2/c$) and compare to the experimental spectrum of Sample 1. We find that the measured XAS spectra are best described by $Nb_2O_5$. The splitting between the two dominant peaks is larger in the crystalline reference samples, while the relative heights of the two dominant peaks is qualitatively described by $Nb_2O_5$, suggesting amorphous structures with $Nb_2O_5$ stoichiometry. We further find that as the oxidation state of the Nb atom increases (+2 in NbO to +5 in $Nb_2O_5$), both the intensity of the first peak increases, and the ratio of the intensity of the first peak to the second peak increases. This is partially explained by considering the resulting filling of the $t_{2g}$ and $e_g$ states of an octahedrally coordinated Nb atom (see inset of Figure 2); NbO deviates slightly from the trend because the coordination of the Nb atoms is square planar.

In Figure 3(b), we compare the calculated XAS spectra for three different crystalline polymorphs and an amorphous structure of stoichiometric $Nb_2O_5$ to the measured XAS of Sample 1. We choose Sample 1 since we anticipate the oxidized film with no additional fabrication steps is most similar to a completely amorphous phase. We find that both the average amorphous spectrum and the crystalline N-phase spectrum are most similar to the experimental spectrum from Sample 1. Of the crystalline phases, we find that the N-phase best agrees with the XAS measurements, but the calculation shows a larger splitting between the two dominant peaks than the measured spectrum. This is the case for all of the considered crystalline phases of $Nb_2O_5$ (Figure 3(b)), which is caused by the crystalline order increasing the crystal field splitting.

Previous works suggest magnetic impurities contribute to impedance-based losses in superconducting qubits.[11,13] In particular, $d$-type magnetic impurities on Nb atoms were found to be more detrimental than $p$-type impurities on O atoms in Nb oxides.[13] To investigate if our XAS measurements can identify a low density of magnetic impurities, we compare our calculated XAS spectra with those measured. We divide our calculations into three groups; stoichiometric $Nb_2O_5$, oxygen rich $Nb_2O_5$ (includes oxygen interstitials or Nb vacancies), and oxygen poor $Nb_2O_5$ (includes oxygen vacancies) with the results given in Figure 4. As expected, we find a pre-edge feature in the oxygen rich calculations coming from O-O dangling bonds, and resulting in the $p$-type magnetic impurities. However, such a pre-peak feature is not observed in any of the measured XAS spectra, so we can conclude that there is not a significant density of $p$-type

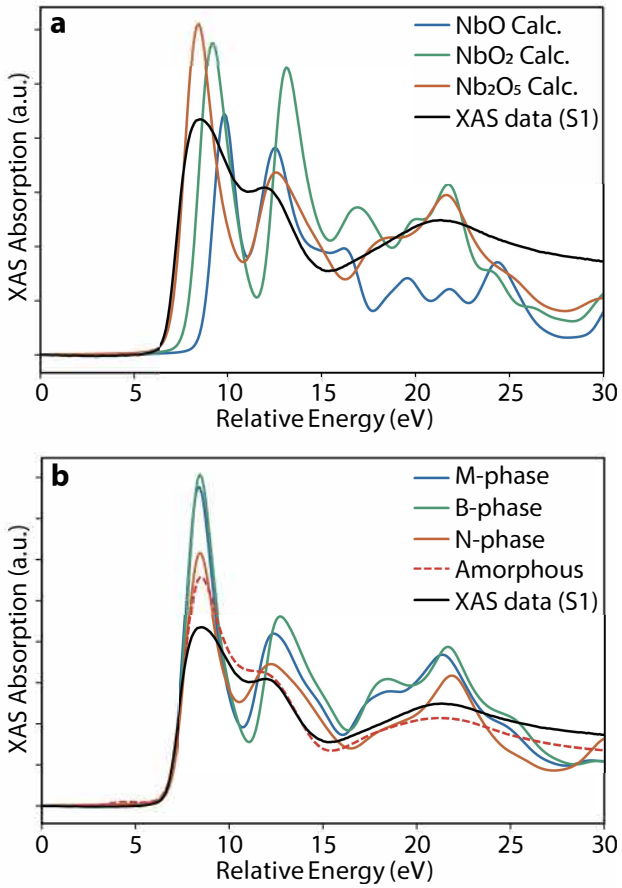


FIG. 3. (a) Calculated XAS spectra for crystalline NbO, $NbO_2$ and $Nb_2O_5$ (averaged over all three calculated phases) and XAS measurements of the O K edge of Sample 1. (b) Calculated XAS spectra for crystalline $Nb_2O_5$ in the M-, B-, and B- phases, a representative *ab initio* generated amorphous structure, and XAS measurements of Sample 1. Experimental data is normalized by rigidly shifting the spectrum to the relative scale, removing the background signal, and normalizing the heights to be comparable to our XAS calculations.

magnetic impurities in our measured samples. We find a slightly better agreement between the oxygen-poor calculated spectra and the measured spectra with shape of the second peak at $\approx$ 13 eV a closer match in this case. This suggests the presence of $d$-type magnetic impurities associated with oxygen poor (and Nb rich) samples. To further quantify this, we perform statistical analysis on the 1250 distinct calculated atomic spectra and compare them to the measured XAS to correlate spectral changes with structural and magnetic changes (details in the SI). These results suggest that small densities of $d$-type magnetic impurities are present in all three measured samples with an estimated density of $1.8\times10^{22}$, $1.7\times10^{22}$, and $1.5\times10^{22}$ $d$-type impurities per mol formed from oxygen vacancies found in Samples 1, 2, and 3, respectively. This density of magnetic moments is higher than previous magnetic measurements on bulk crystalline $T$- and $TT$-$Nb_2O_5$ where they estimated a density of

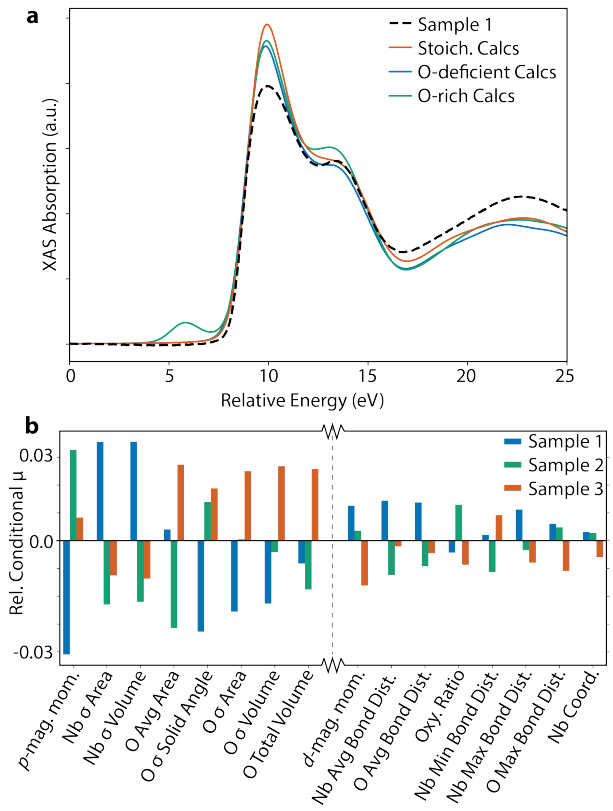


FIG. 4. (a) Comparison between stoichiometric, oxygen-deficient, and oxygen-rich amorphous calculated spectra versus the experimental spectrum of sample 1. (b) Statistical analysis of the expected relative changes in structural descriptors given the three experimental XAS spectra. The highest variance descriptors are on the left and lowest variance descriptors are on the right.

$10^{21}$ – $10^{22}$ effective magnetic moments per mol.[37] However, the greater density of magnetic moments in our samples is consistent with the increased disorder and off-stoichiometry that we expect in our amorphous surface oxides. To elucidate the structural changes amongst the different samples that are correlated with changes in the XAS spectra, we calculate the conditional mean for each structural and magnetic descriptor given to the experimental spectrum. The relative expected changes for the most and least varying descriptors are plotted in Figure 4(b). The shape descriptors (volume, area, etc.) refer to Voronoi polyhedra constructed around each atom, $\sigma$ values refer to distortions within those descriptors (full descriptions are in the SI). We find that the fabrication procedure has a reasonably large effect on the $p$-type impurity density along with the shape descriptors of both Nb and O atoms. Bond length and coordination characteristics along with $d$-type impurity density showed less variation amongst the samples.

In summary,our FEM measurements confirm the lack of long-range order in a representative Nb-oxide film, observed from the broad halo in the average speckle pattern of the FEM image. Comparing the calculated RDF of our *ab initio*-generated stoichiometric $Nb_2O_5$ amorphous structures to the angular average of the FEM pattern indicates that our generated amorphous configurations are a good representation of the distribution of structures observed in real Nb-oxide films, containing a mix of edge and corner-sharing polyhedra motifs. We next compared our measured XAS spectra for a selection of Nb-oxide samples (Table I) to first-principles calculations of both crystalline and amorphous Nb-oxide compounds, of which the amorphous phase most closely matched the data, which isconsistent with our FEM results, and prior elemental analysis of Nb-oxide films.[19] Finally, we analyze our first-principles predictions for signatures of magnetic impurities in the amorphous configurations to identify experimental markers of these magnetic impurities in the XAS spectra. We find a better fit of the XAS spectra for $Nb_2O_5$ configurations with oxygen vacancies, suggesting the presence of $d$-type magnetic impurities. We find no evidence for pre-edge impurity states associated with $p$-type magnetic impurities. Our results give an estimate of the density of decoherence-inducing local magnetic moments, and suggest experimental fingerprints for the characterization of superconducting thin films using spectroscopic approaches.

## DATA AVAILABILITY

The data that support the findings of this study are openly available in Zenodo at Ref.[38]

## SUPPLEMENTARY MATERIAL

See supplementary material for details of our FEM and XAS measurements along with our calculation parameters and further details of our machine learning model.

## ACKNOWLEDGMENTS

We thank John Clarke and David Santiago for useful discussions. Specific software and hardware is identified for information purposes only and is not intended to imply recommendation or endorsement by NIST. This work was funded by the U.S. Department of Energy, Office of Science, Office of Basic Energy Sciences, Materials Sciences and Engineering Division under Contract No. DE-AC02-05-CH11231 "High-Coherence Multilayer Superconducting Structures for Large Scale Qubit Integration and Photonic Transduction program (QIS-LBNL)". This research used resources of the National Energy Research Scientific Computing Center (NERSC), a U.S. Department of Energy Office of Science User Facility located at Lawrence Berkeley National Laboratory, operated under Contract No. DE-AC02-05CH11231. E.S. acknowledges support from the US-Irish Fulbright Commission,

the Air Force Office of Scientific Research under award number FA9550-18-1-0480 and the EPSRC Centre for Doctoral Training in Cross-Disciplinary Approaches to Non-Equilibrium Systems (EP/L015854/1). This work also used the Extreme Science and Engineering Discovery Environment (XSEDE), which is supported by National Science Foundation grant number ACI-1548562. Electron microscopy data acquisition for this work was supported by National Science Foundation STROBE Grant No. DMR-1548924. Work at the Molecular Foundry was supported by the Office of Science, Office of Basic Energy Sciences, of the U.S. Department of Energy under Contract No. DE-AC02-05CH11231. This research used resources of the Advanced Light Source, which is a DOE Office of Science User Facility under Contract no. DE-AC02-05CH11231.

## AUTHOR DECLARATIONS

The authors have no conflicts to disclose.

[1] M. H. Devoret and R. J. Schoelkopf, "Superconducting circuits for quantum information: an outlook," Science **339**, 1169–1174 (2013).

[2] M. Kjaergaard, M. E. Schwartz, J. Braumüller, P. Krantz, J. I.-J. Wang, S. Gustavsson, and W. D. Oliver, "Superconducting qubits: Current state of play," Annual Review of Condensed Matter Physics **11**, 369–395 (2020).

[3] R. McDermott, "Materials origins of decoherence in superconducting qubits," IEEE Trans. Appl. Supercond. **19**, 2–13 (2009).

[4] W. D. Oliver and P. B. Welander, "Materials in superconducting quantum bits," MRS Bull. **38** (2013), 10.1557/mrs.2013.229.

[5] N. P. de Leon, K. M. Itoh, D. Kim, K. K. Mehta, T. E. Northup, H. Paik, B. S. Palmer, N. Samarth, S. Sangtawesin, and D. W. Steuerman, "Materials challenges and opportunities for quantum computing hardware," Science **372** (2021), 10.1126/science.abb2823.

[6] C. Müller, J. H. Cole, and J. Lisenfeld, "Towards understanding two-level-systems in amorphous solids: Insights from quantum circuits," Reports on Progress in Physics **82**, 1–34 (2019).

[7] W. A. Phillips, "Two-level states in glasses," Rep. Prog. Phys. **50**, 1657–1708 (1987).

[8] J. Burnett, L. Faoro, and T. Lindström, "Analysis of high quality superconducting resonators: consequences for TLS properties in amorphous oxides," Supercond. Sci. Technol. **29**, 044008 (2016).

[9] C. D. Wilen, S. Abdullah, N. A. Kurinsky, C. Stanford, L. Cardani, G. D'Imperio, C. Tomei, L. Faoro, L. B. Ioffe, C. H. Liu, A. Opremcak, B. G. Christensen, J. L. DuBois, and R. McDermott, "Correlated charge noise and relaxation errors in superconducting qubits," (2020), arXiv:2012.06029 [quant-ph].

[10] L. Cardani, F. Valenti, N. Casali, G. Catelani, T. Charpentier, M. Clemenza, I. Colantoni, A. Cruciani, L. Gironi, L. Grünhaupt, D. Gusenkova, F. Henriques, M. Lagoin, M. Martinez, G. Pettinari, C. Rusconi, O. Sander, A. V. Ustinov, M. Weber, W. Wernsdorfer, M. Vignati, S. Pirro, and I. M. Pop, "Reducing the impact of radioactivity on quantum circuits in a deep-underground facility," (2020), arXiv:2005.02286 [cond-mat.supr-con].

[11] M. Kharitonov, T. Proslier, A. Glatz, and M. J. Pellin, "Surface impedance of superconductors with magnetic impurities," Phys. Rev. B Condens. Matter **86**, 024514 (2012).

[12] T. Proslier, M. Kharitonov, M. Pellin, J. Zasadzinski, and Ciovati, "Evidence of surface paramagnetism in niobium and consequences for the superconducting cavity surface impedance," IEEE Trans. Appl. Supercond. **21**, 2619–2622 (2011).

[13] E. Sheridan, T. F. Harrelson, E. Sivonxay, K. A. Persson, M. V. P. Altoe, I. Siddiqi, D. F. Ogletree, D. I. Santiago, and S. M. Griffin, "Microscopic theory of magnetic Disorder-Induced decoherence in superconducting nb films," (2021).

[14] A. P. Vepsäläinen, A. H. Karamlou, J. L. Orrell, A. S. Dogra, B. Loer, F. Vasconcelos, D. K. Kim, A. J. Melville, B. M. Niedzielski, J. L. Yoder, S. Gustavsson, J. A. Formaggio, B. A. VanDevender, and W. D. Oliver, "Impact of ionizing radiation on superconducting qubit coherence," Nature **584**, 551–556 (2020).

[15] J. M. Martinis, "Saving superconducting quantum processors from qubit decay and correlated errors generated by gamma and cosmic rays," (2020), arXiv:2012.06137 [quant-ph].

[16] A. P. M. Place, L. V. H. Rodgers, P. Mundada, B. M. Smitham, M. Fitzpatrick, Z. Leng, A. Premkumar, J. Bryon, A. Vrajitoarea, S. Sussman, G. Cheng, T. Madhavan, H. K. Babla, X. H. Le, Y. Gang, B. Jäck, A. Gyenis, N. Yao, R. J. Cava, N. P. de Leon, and A. A. Houck, "New material platform for superconducting transmon qubits with coherence times exceeding 0.3 milliseconds," Nat. Commun. **12**, 1779 (2021), arXiv:2003.00024 [quant-ph].

[17] S. B. Kaplan, C. Chi, D. Langenberg, J.-J. Chang, S. Jafarey, and D. Scalapino, "Quasiparticle and phonon lifetimes in superconductors," Physical Review B **14**, 4854 (1976).

[18] M. Delheusy, A. Stierle, N. Kasper, R. Kurta, A. Vlad, H. Dosch, C. Antoine, A. Resta, E. Lundgren, and J. Andersen, "X-ray investigation of subsurface interstitial oxygen at nb/oxide interfaces," Applied Physics Letters **92**, 101911 (2008).

[19] M. V. P. Altoé, A. Banerjee, C. Berk, A. Hajr, A. Schwartzberg, C. Song, M. A. Ghadeer, S. Aloni, M. J. Elowson, J. M. Kreikebaum, E. K. Wong, S. Griffin, S. Rao, A. Weber-Bargioni, A. M. Minor, D. I. Santiago, S. Cabrini, I. Siddiqi, and D. F. Ogletree, "Localization and reduction of superconducting quantum coherent circuit losses," (2020), arXiv:2012.07604.

[20] M. Mergenthaler, S. Paredes, P. Müller, C. Müller, S. Filipp, M. Sandberg, J. Hertzberg, V. P. Adiga, M. Brink, and A. Fuhrer, "Ultrahigh vacuum packaging and surface cleaning for quantum devices," Review of Scientific Instruments **92**, 025121 (2021).

[21] J. Verjauw, A. Potočnik, M. Mongillo, R. Acharya, F. Mohiyaddin, G. Simion, A. Pacco, T. Ivanov, D. Wan, A. Vanleenhove, *et al.*, "Investigation of microwave loss induced by oxide regrowth in high-q niobium resonators," Physical Review Applied **16**, 014018 (2021).

[22] A. Romanenko and D. I. Schuster, "Understanding quality factor degradation in superconducting niobium cavities at low microwave field amplitudes," Phys. Rev. Lett. **119**, 264801 (2017).

[23] A. Romanenko, R. Pilipenko, S. Zorzetti, D. Frolov, M. Awida, S. Belomestnykh, S. Posen, and A. Grassellino, "Three-Dimensional superconducting resonators at $T < 20$ mk with photon lifetimes up to $\{\tau\} = 2$ s," Phys. Rev. Applied **13**, 034032 (2020).

[24] B. W. Heinrich, J. I. Pascual, and K. J. Franke, "Single magnetic adsorbates on s-wave superconductors," Progress in Surface Science **93**, 1–19 (2018).

[25] P. Voyles and D. Muller, "Fluctuation microscopy in the STEM," Ultramicroscopy **93**, 147–159 (2002).

[26] G. Kresse and J. Hafner, "Ab initio molecular dynamics for liquid metals," Physical Review B **47**, 558–561 (1993).

[27] T. F. Harrelson, E. Sheridan, E. Sivonxay, K. A. Persson, and S. M. Griffin, "Amorphous Niobium Oxide Structures Calculated from First Principles using Density Functional Theory and Molecular Dynamics," (2021), 10.5281/ZENODO.5139270.

[28] J. Vinson, J. J. Rehr, J. J. Kas, and E. L. Shirley, "Bethe-salpeter equation calculations of core excitation spectra," Phys. Rev. B **83**, 115106 (2011); K. Gilmore, J. Vinson, E. Shirley, D. Prendergast, C. Pemmaraju, J. Kas, F. Vila, and J. Rehr, "Efficient implementation of core-excitation bethe-salpeter equation calculations," Comput. Phys. Comm. **197**, 109 – 117 (2015); `www.ocean-code.com` *v* 2.9.7.

[29]P. Giannozzi, O. Andreussi, T. Brumme, O. Bunau, M. B. Nardelli, M. Calandra, R. Car, C. Cavazzoni, D. Ceresoli, M. Cococcioni, N. Colonna, I. Carnimeo, A. D. Corso, S. de Gironcoli, P. Delugas, R. A. DiStasio, A. Ferretti, A. Floris, G. Fratesi, G. Fugallo, R. Gebauer, U. Gerstmann, F. Giustino, T. Gorni, J. Jia, M. Kawamura, H.-Y. Ko, A. Kokalj, E. Küçükbenli, M. Lazzeri, M. Marsili, N. Marzari, F. Mauri, N. L. Nguyen, H.-V. Nguyen, A. O. de-la Roza, L. Paulatto, S. Poncé, D. Rocca, R. Sabatini, B. Santra, M. Schlipf, A. P. Seitsonen, A. Smogunov, I. Timrov, T. Thonhauser, P. Umari, N. Vast, X. Wu, and S. Baroni, "Advanced capabilities for materials modelling with quantum ESPRESSO," Journal of Physics: Condensed Matter **29**, 465901 (2017); `www.quantum-espresso.org` *v* 6.7.

[30]M. van Setten, M. Giantomassi, E. Bousquet, M. Verstraete, D. Hamann, X. Gonze, and G.-M. Rignanese, "The pseudodojo: Training and grading a 85 element optimized norm-conserving pseudopotential table," Computer Physics Communications **226**, 39 – 54 (2018); `http://www.pseudo-dojo.org` Scalar-relativstic *v.* 0.4.

[31]D. R. Hamann, "Optimized norm-conserving vanderbilt pseudopotentials," Phys. Rev. B **88**, 085117 (2013); The open-source code ONCVPSP is avaiable at `http://www.mat-simresearch.com` *v.* 3.3.1.

[32]P. M. Voyles and J. R. Abelson, "Medium-range order in amorphous silicon measured by fluctuation electron microscopy," Solar energy materials and solar cells **78**, 85–113 (2003).

[33]T. Daulton, K. Bondi, and K. Kenneth, "Nanobeam diffraction fluctuation electron microscopy technique for structural characterization of disordered materials — application to $Al_88 - xY_7Fe_5Ti_x$ metallic glasses," Ultramicroscopy **110**, 1279–1289 (2010).

[34]E. Kennedy, N. Reynolds, L. Rangel DaCosta, F. Hellman, C. Ophus, and M. Scott, "Tilted fluctuation electron microscopy," Applied Physics Letters **117**, 091903 (2020).

[35]J. Hwang and P. Voyles, "Variable resolution fluctuation electron microscopy on cu-zr metallic glass using a wide range of coherent stem probe size," Microscopy and Microanalysis **17**, 67–74 (2011).

[36]F. Frati, M. O. Hunault, and F. M. de Groot, "Oxygen k-edge x-ray absorption spectra," Chemical reviews **120**, 4056–4110 (2020).

[37]L. K. Herval, D. Von Dreifus, A. C. Rabelo, A. D. Rodrigues, E. C. Pereira, Y. G. Gobato, A. J. De Oliveira, and M. P. De Godoy, "The role of defects on the structural and magnetic properties of $Nb_2O_5$," Journal of Alloys and Compounds **653**, 358–362 (2015).

[38]T. F. Harrelson, J. Vinson, E. Sheridan, and S. M. Griffin, "Calculated O K-edge XAS Spectra of Niobium Oxide Phases using Bethe-Salpeter equation," (2021), 10.5281/ZENODO.5156863.